Ethanol Electro-Oxidation on Ternary Platinum–Rhodium–Tin Nanocatalysts: Insights in the Atomic 3D Structure of the Active Catalytic Phase

Nina Erini,[†,#] Rameshwori Loukrakpam,[†,#] Valeri Petkov,[‡] Elena A. Baranova,[§] Ruizhi Yang,[‖] Detre Teschner,[⊥] Yunhui Huang,[#] Stanko R. Brankovic,[●] and Peter Strasser*,[†]

[†]Department of Chemistry, Chemical Engineering Division, Technical University Berlin, 10623 Berlin, Germany

[‡]Department of Physics, Central Michigan University, 1200 South Franklin Street, Mt. Pleasant, Michigan 48859, United States

[§]Department of Chemical and Biological Engineering, Centre for Catalysis Research and Innovation (CCRI), University of Ottawa, 161 Louis Pasteur, Ottawa, ON K1N6N5, Canada

[‖]School of Energy, Soochow University, No. 1 Shizi Street, Suzhou, Jiangsu 215006, China

[⊥]Department of Inorganic Chemistry, Fritz-Haber-Institute of the Max Planck Society, Faradayweg 4–6, 14195 Berlin, Germany

[#]School of Materials Science and Engineering, Huazhong University of Science and Technology, 1037 Luoyu Road, Wuhan, 430074, China

[●]Department of Electrical and Computer Engineering, University of Houston, N308 Engineering Building 1, Houston, Texas 77204, United States

ⓢ *Supporting Information*

ABSTRACT: Novel insights in the synthesis–structure–catalytic activity relationships of nanostructured trimetallic Pt–Rh–Sn electrocatalysts for the electrocatalytic oxidation of ethanol are reported. In particular, we identify a novel single-phase Rh-doped Pt–Sn Niggliite mineral phase as the source of catalytically active sites for ethanol oxidation; we discuss its morphology, composition, chemical surface state, and the detailed 3D atomic arrangement using high-energy (HE-XRD), atomic pair distribution function (PDF) analysis, and X-ray photoelectron spectroscopy (XPS). The intrinsic ethanol oxidation activity of the active Niggliite phase exceeded those of earlier reports, lending support to the notion that the atomic-scale neighborhood of Pt, Rh, and Sn is conducive to the emergence of active surface catalytic sites under reaction conditions. In situ mechanistic Fourier transform infrared (in situ FTIR) analysis confirms an active 12 electron oxidation reaction channel to CO_2 at electrode potentials as low as 450 mV/RHE, demonstrating the favorable efficiency of the PtRhSn Niggliite phase for C–C bond splitting.

KEYWORDS: *ethanol oxidation reaction, fuel cells, electrochemistry, electrocatalysis, HE-XRD, PDF analysis, in situ FTIR*
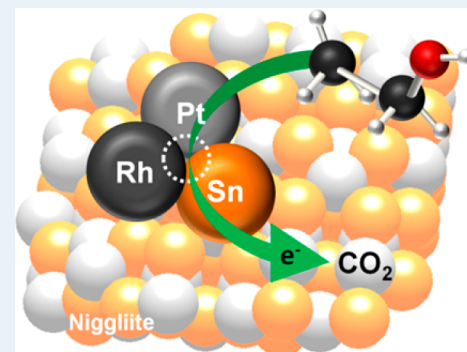
1. INTRODUCTION

Development of direct ethanol fuel cells (DEFCs) as alternate power sources has been a subject of intensive studies for fundamental and practical applications (e.g., the development of compact portable power as well as electric vehicle range extenders operating at high temperatures).[1−4] Liquid fuels, like low carbon alcohols, such as methanol or ethanol, have higher volumetric and gravimetric energy densities, better energy efficiencies, and they offer easy handling, storage, and transportation, contrary to gaseous fuels.[5] Although methanol is of a particular interest for mobile applications such as electric vehicles, ethanol has some important advantages over methanol such as higher energy density (8 kWh kg^{-1} vs 6 kWh kg^{-1}, respectively), low toxicity, biocompatibility, and abundant availability. It is, however, not as easily oxidized to CO_2 and water as methanol. This is attributed to difficulties in the sluggish adsorption and cleavage of C–C bonds in ethanol and, by some authors, to the formation of CO intermediates leading to poisoning of the active sites on Pt catalysts.[6−9] Complete ethanol electro-oxidation to CO_2 involves 12 electrons per molecule, whereas partial oxidation leads to byproducts like acetic acid or acetaldehyde, which reduce the Faradaic efficiency of the anodic reaction of DEFC. Efforts to develop highly active and selective electrocatalysts for the ethanol oxidation reaction (EOR) to CO_2 have therefore concentrated on the addition of cocatalysts to platinum.[10] The most promising family of EOR nanocatalysts are currently based on mixtures of Pt, Rh, and Sn.[8,11−16] However, the optimal

structural arrangement of the atoms of the three components in the surface and bulk of the final active catalyst to maximize activity and selectivity have not been clarified to date at an atomic scale.

Mechanistic details of the Rh and Sn-promoted oxidation of ethanol on Pt are also not well understood. It is believed that Rh increases the yield of CO_2 by promoting the C−C bond cleavage. However, there is reason that this hypothesis does not represent a comprehensive picture of the role of Rh in this family of catalysts. The role of Sn in the ternary Pt−Rh−Sn electrocatalysts is even more controversial.

A large number of previous studies have primarily focused on the effects of either alloying Sn into Pt[9,17,18] or on the presence of SnO_2 species.[19−21] SnO_2 is well-known for being potentially able to provide O species for the oxidation of intermediates produced during the dissociative adsorption of ethanol on Pt active sites (bifunctional mechanism).[22] Adzic et al.[8] prepared an active $PtRhSnO_2/C$ ethanol electrocatalysts using electrochemical underpotential deposition (UPD) of Pt and Rh atoms on carbon-supported SnO_2 nanoparticles in a fairly complex multistep process. The authors used X-ray absorption to learn about local Pt and Rh coordination and bond lengths; however, they did not address the 3D atomic arrangement of their active "quasi-random alloy".

In a more recent report, Kowal et al. reported on a set of Pt−Rh−SnO_2 nanoparticle catalysts and proposed twinned Pt−Rh and SnO_2 crystallites with an optimal Pt/Rh/Sn = 3:1:4 ratio.[12,15] As most authors, they gave no particular attention to the effect of the order of addition of the components. The catalytic effect of different metal ratios was also studied by Garcia-Rodriguez et al. by adding various amounts of Rh to a carbon-supported Pt_3Sn ethanol electrocatalysts.[16] Du et al. reported the synthesis of carbon-supported $PtRhSnO_2$ nanoclusters with simultaneous reduction of the precursor salts. This study reported two coexisting Sn phases in the $Pt_{52}Rh_{12}Sn_{36}$ material: metallic Sn in a PtRhSn homogeneous alloy and SnO_2 as a secondary phase.[23] Spinacé et al. reported PtSnRh/C electrocatalysts synthesized via an alcohol-reduction process using ethylene glycol and showed that this ternary catalyst and binary PtSn/C performed similarly for ethanol oxidation at RT, whereas the activity of binary PtRh/C electrocatalysts was very low. However, at 100 °C the ternary catalyst was found to exhibit superior performance compared to the two binary relatives.[13] Lastly, Silva et al. reported a nonalloyed PtSn catalyst claiming preferred C−C bond cleavage. That catalyst showed conversion of ethanol to CO_2 but the conversion kinetics was prohibitively slow at practical DEFC anode potentials.[14]

A consensus is emerging that the catalytic activity of ternary Pt−Rh−Sn materials is generally superior to that of their binary relatives. However, important structural insights about the catalytically active bulk and surface phase are missing; in particular, the detailed three-dimensional atomic arrangement of the Pt, Rh, and Sn atoms of the active catalytic phase has remained unresolved, and so has the question whether crystalline homogeneous single phase materials, crystalline multiphase materials, or even phases with limited structural coherence (partially amorphous phases) are preferred. What adds to the confusion caused by the conflicting reports on the catalytic activity of ternary $PtRhSnO_2$ catalysts is the fact that no one has ever paid closer attention as to how the sequence of addition of the three metal components affects catalyst structure and activity. In other words, it is not clearly documented what detailed synthesis protocol was *actually conducive* for high catalytic activity and high CO_2 selectivity.

To address some of these questions and to gain better understanding of the desired 3D atomic arrangement of Pt, Rh, and Sn in active EOR catalysts, we prepared a variety of different ternary Pt−Rh−Sn nanoparticle catalysts by varying the sequence in which each metal component entered the synthetic process of the final catalyst material. A comprehensive set of real and reciprocal space techniques was employed to explore composition, morphology, and atomic-scale structural coherence, most prominently synchrotron-based high-energy X-ray diffraction (HE-XRD), transmission electron microscopy (TEM) coupled with energy disperse X-ray spectroscopy (EDS), as well in situ Fourier transform infrared spectroscopy (in situ FTIR). What sets this study apart from earlier structural investigations is the exploration of structural coherence using the atomic pair distribution function (PDF) analysis. This clearly underutilized yet powerful tool yields the PDF, which represents the degree and length of structural coherence and provides insight in the interatomic distances and atomic coordination shells incorporating contributions of both ordered and amorphous domains. The modeling of experimental PDFs provided us with structural motifs of the catalytically active phase. On the basis of our PDF analysis, we find that a novel single-phase ternary PtRhSn electrocatalysts displaying a Niggliite-type mineral structure with good structural coherence possesses high crystallinity and single phase ternary structure. XPS analysis confirms the presence of surface Sn oxide species, as can be expected for a non-noble metal as Sn in acidic solutions. This provides a high concentration of active sites on the catalyst surface, where Pt and Rh in their reduced state are in direct contact with oxidized Sn in order to exhibit the highest and most selective EOR activities toward the complete 12 electron oxidation of ethanol to CO_2, in sharp contrast with unalloyed phase separated nanocatalysts.

2. EXPERIMENTAL SECTION

2.1. Synthesis of PtRhSn Nanoparticle Catalysts. The following chemicals were used for the nanoalloy catalysts synthesis: platinum(II) 2,4 pentadionate (Pt 99.0% min, Alfa Aesar), rhodium(II) acetate, dimer (98+%, Alfa Aesar), tin(II) acetylacetonate dimer (98.0%, Alfa Aesar), 1,2 tetradecandiol (90% Aldrich), oleic acid (90%, Alfa Aesar), oleylamine (70%, Aldrich), dioctylether (99%, Aldrich), *n*-hexane (ROTIPURAN ≥99%, p.a., ACS, Carl Roth), and Ketjenblack EC600JD (AkzoNobel) as carbon support. In all synthesis methods of the ternary electrocatalysts, the same amount of precursors, reducing and capping agents were used to maintain an atomic ratio of 3:1:4 (Pt/Rh/Sn). Five different catalysts are prepared as follows

PtRhSn/C. For preparation of the PtRhSn/C catalyst, 351.97 mg (0.89 mmol) of $Pt(acac)_2$, 75.25 mg (0.34 mmol) of $Rh(ac)_2$, and 0.48 mL (1.36 mmol) of $Sn(acac)_2$, respectively, as well as 622.47 mg (2.70 mmol) TDD (1,2 tetradecandiol), 0.48 mL (1.5 mmol) of OAc (oleic acid), and 0.50 mL (1.5 mmol) of OAm (oleylamine) are dissolved in 60 mL of dioctylether. The mixture is stirred at 800 rpm while it is heated to 260 °C for 30 min. To produce a simultaneously reduced PtRhSn/C, all precursors were mixed together from the beginning of the reaction.

PtRh/C. Pt and Rh precursors were mixed together in a ratio of 3:1, and a similar reaction protocol as for PtRhSn/C is

employed where the two precursors were reduced simultaneously.

Sn+Rh+Pt/C. The Sn+Rh+Pt/C catalyst was synthesized by the reduction of Sn precursor in TDD in the presence of OAc and OAm in dioctylether, followed by heating up to 260 °C and cooling down to room temperature (RT). Then, the Rh precursor was added with the other half of TDD, OAc, and OAm for reduction at 260 °C and cooling to RT. Subsequently, Pt precursor was added for reduction in the mixture consecutively.

Sn+RhPt/C. The Sn+RhPt/C catalyst was synthesized by the reduction of Sn precursor at 260 °C, cooling to RT, and then, reduction of both Pt and Rh precursor in the mixture at the same time in a pseudoconsecutive process.

Sn+Pt/C. The Sn+Pt/C catalyst was produced by adding Sn precursor to half of TDD, OAc, and OAm, followed by heating up to 260 °C and cooling down to RT. Then the Pt precursor was added with the other half of TDD, OAc, and OAm followed by heating and cooling as described above in a consecutive reduction process of the two precursors.

In all syntheses, the reaction mixtures were cooled and precipitated with 100 mL of isopropanol overnight in dark. The precipitated nanoparticles were separated by centrifugation and then redispersed in *n*-hexane. Ketjen black (300 mg) was dispersed in 100 mL *n*-hexane and sonicated on ice for 60 min. Two-thirds of the NPs suspension in *n*-hexane (equivalent to ~300 mg of NPs) was added to the carbon suspension, and the mixture was sonicated on ice for another 60 min and then stirred overnight at RT. To obtain carbon-supported catalysts, the mixture was centrifuged, separated from the solution, and the residue was dried in a furnace under N_2 (ramp = 4 °C/min to 280 °C, held for 1 h, and cooled to RT under N_2 overnight). Half of the dried NPs/C was oxidized under O_2/N_2 in the furnace (ramp = 4 °C/min to 250 °C, held for 2 h and cooled to RT under O_2/N_2). A calcination step was followed by heating under H_2/Ar atmosphere (ramp 5 °C/min to 400 °C, held for 1 h, and cooled to RT under H_2/Ar).

2.2. Physico-Chemical Characterization of Catalysts. *Inductively Coupled Plasma-Optical Emission Spectroscopy (ICP-OES).* ICP-OES was used for compositional analysis. It was performed using a 715-ES-inductively coupled plasma analysis system (Varian). Six milligrams of each catalyst was suspended in 2 mL aqua regia and stirred for 1 h to let the acidic fumes out. The mixture was diluted with miliQ water to 10 mL, heated under pressure in a microwave (CEM Discover, 10 min ramp, 180 °C, 20 min hold), and consecutively diluted to two concentrations that were calibrated to a blank and three standards. Catalyst compositions were determined by the concentration, metal loading from the difference of metal content and initial mass, assuming the catalysts contained only Pt, Sn, and Rh. The standard concentrations were the following: 5, 10, and 25 ppm for Pt; 3, 10, and 20 ppm for Sn; and 1, 3, and 10 ppm for Rh. The chosen wavelengths for analysis were 265.9 nm for Pt, 343.5 nm for Rh, and 189.9 nm for Sn.

Transmission Electron Microscopy (TEM) and Energy Dispersive X-ray Spectroscopy (EDX). Both TEM and EDX were used to study morphology and composition. A small amount of the electrocatalysts was dispersed via ultrasonication in 0.5 mL of hexane. A Cu grid coated with holey carbon film was impregnated with 2 *μ*L of the solution and air-dried. A FEI TECNAI G² 20 S-TWIN microscope, equipped with a GATAN MS794 P CCD-detector operated at 200 kV was used. The

mean particle size was determined from the TEM images by counting of 50—200 particles. EDX data were collected for 120 s at an angle of 45° with respect to the sample holder.

Cu Kα X-ray Diffraction. Diffraction patterns were collected using a D8 Advance diffractometer (Bruker) equipped with a Lynx Eye Detector and a KFL Cu 2K X-ray tube. The diffraction patterns were collected in a 20—80° 2θ range with a step size of 0.00142° dwelling for 30 s at every step. The XRD patterns were analyzed using the MDI Jade 8 software package. Bragg peak positions were compared with the reference XRD patterns (PDF data files, National Institute of Science and Technology).

High-Energy X-ray Diffraction (HE-XRD) and Pair Distribution Function (PDF) Analysis. Measurements were performed for electrocatalysts sealed inside glass capillaries on beamline 11IDC at the Advanced Photon Source, Argonne National Laboratory, USA, using synchrotron X-ray of 0.1080 Å wavelength. The diffraction data were reduced to the so-called structure factors, $S(q)$, and then Fourier transformed to the corresponding atomic PDFs $G(r)$, using the relationship:

$$G(r) = \frac{2}{\pi} \int_{q=0}^{q_{max}} q[S(q) - 1]\sin(qr)\,dq$$

where $q_{max} = 25$ Å^{-1} in the present experiments. The wave vector q is defined as $q = 4\pi\sin(\theta)/\lambda$, where θ is half of the scattering angle and λ is the wavelength of the X-rays used. Note, as derived, atomic PDFs $G(r)$ are experimental quantities that oscillate around zero and show positive peaks at real space distances, r, where the local atomic density $\rho(r)$ exceeds the average one ρ_o. This behavior can be expressed by the equation $G(r) = 4\pi r\rho_o[\rho(r)/\rho_o - 1]$, which is the formal definition of the PDF $G(r)$.[24]

In Situ Fourier Transform Infrared Spectroscopy (In Situ FTIR). In situ FTIR was measured using a NICOLET 6700 FTIR apparatus equipped with a MCT-A detector cooled with liquid nitrogen. The compartments were purged using compressed air free of CO_2 and H_2O at an inlet pressure of 60 psi from a Parker Balston Purge Gas Generator operating at a flow rate of 9 L/min. The electrode potential was controlled by BAS CV-27 potentiostat. A custom-made spectro-electro-chemical Teflon cell with a hemispherical ZnSe window was connected to the optical window (ZnSe) via a Teflon tape. An ink made of the electrocatalyst suspended in ultrapure water, isopropanol, and nafion was put as a film on a polished Au(100) single-crystal operating as the working electrode (WE), which was placed together with the reference electrode (SCE) and counter electrode (Pt wire) in the cell filled with the electrolyte (0.1 M $HClO_4$ + 0.5 M C_2H_5OH). The WE was pushed against the optical window under 0.05 V versus RHE to achieve appreciable increase of interferogram peak-to-peak signal. Afterward, the sample compartment was closed, and dry compressed N_2 was purged for 2 h to eliminate water and CO_2 from the spectrometer compartment. The background spectrum was collected at 0.15 V, and the potential was stepped by 0.10 V in positive direction to 1.15 V. At each potential, interferograms were collected at 8 cm^{-1} resolution with 128 scans, with 20 s of delay between setting (potential switch) and measurements to allow the interface to reach equilibrium. The interferograms were processed using OMNIC software to obtain characteristic spectra. Spectra were obtained by subtractively normalized interfacial Fourier transform infrared spectroscopy (SNIFTIRS). During a typical SNIFTIRS, the electrode potential was modulated between

values E1, sample potential (usually potential for strong adsorption of probe molecules or production of intermediates) and E2, background potential (where there is no adsorption of probe molecule). The spectrum is obtained by the following equation:

$$\frac{\Delta R}{R} = \frac{R(E2) - R(E1)}{R(E1)}$$

where the difference between two single beam reflectivities (R) at applied potentials E1 and E2 is related to the reflectivity at potential E1. The goal of computing this difference (normalized) spectra is to obtain spectra of surface-bound intermediates, essentially free from bulk contribution. The SNIFTIRS method is part of the external reflection configuration used to study structural aspects of the adsorption processes.[25]

X-ray Photoelectron Spectroscopy. PtRhSn/C catalysts were studied using X-ray photoelectron spectroscopy (XPS) at photon energies yielding electron kinetic energies of 550 eV at the ISISS beamline of the synchrotron facility BESSY of the Helmholtz-Zentrum Berlin. Samples were mounted onto a sapphire sample holder and introduced into the spectrometer. Experiments were carried out at RT in ultrahigh vacuum (UHV). To calculate elemental ratios, the peak areas of Pt 4f, Rh 3d, and Sn 3d were corrected considering the photon flux and tabulated cross sections. To prepare the samples, PtRhSn/C was suspended and sonicated in 0.5 M H_2SO_4 solution for 60 min and then freeze-dried. PtRhSn/C before (BAE) and after (AAE) acid exposure were then dispersed in 4 mL of H_2O and 1 mL of isopropanol with 40 μL of Nafion solution using ultrasonication. This suspension was dropped on the silica surface and dried in air.

Electrochemical Cell. All electrochemical measurements were carried out at RT using a Biologic SP 150 (Biologic) potentiostat. Experiments were carried out in a three-compartment electrochemical glass cell. The electrolytes were deaerated with high-purity N_2 gas (99.998% Linde, Germany) before every measurement. During the experiments, N_2 was purged over the electrolyte through the working electrode compartment. A large surface area Pt counter electrode was contained in a separate compartment. A saturated mercury–mercury sulfate electrode (MMS) was inserted in a separate compartment of the cell via a Luggin capillary for setting desired overpotentials. All potentials reported here are given in respect to a reversible hydrogen electrode (RHE). Sulfuric acid (AnalaR NORMAPUR@ACS, 95%), ethanol (Commercial Alcohols, Inc., 100% ACS grade) and ultrapure water (18 MΩ cm. Millipore) were used to prepare the solutions.

Working Electrode Preparation. Catalyst inks were prepared by dispersing 6 mg of electrocatalyst powder in a mixture of 2.5 mL of ultrapure water, 0.5 mL of isopropanol, and 20 μL of 5 wt % Nafion solution (Aldrich). The mixture was ultrasonicated for 15 min. A glassy carbon disc electrode (GC-DE) (0.196 cm^2 geometrical surface area, Pine Research Instrumentation Company) was used as a support for the catalyst ink. Prior to use, the GC electrodes were prepared by polishing using a Nylon PSA sheet and 5 μm of α-alumina micropolish (0.10 mm) followed by a Microloth sheet and α-alumina micropolish (0.05 mm). The polished electrodes were rinsed thoroughly in ultrapure water and ethanol and then coated with 10 μL of a catalyst ink solution and dried in air, first at RT for 30 min and afterward at 50 °C for 15 min.

Electrochemical Testing. Starting from open circuit potential, cyclic voltammograms (CVs) were carried out in 0.5 M H_2SO_4 to evaluate the hydrogen underpotential (H_{UPD}) charges between 0.05 and 0.4 V versus RHE. EOR polarization curves (linear sweep voltammograms, LSVs) were collected in an electrolyte of 0.5 M C_2H_5OH + 0.5 M H_2SO_4. Potential limits were adjusted between 0.05 and 0.80 V for 20 cycles at 100 mV·s^{-1} and then recorded for five cycles at 20 mV·s^{-1}. Here the second cycle is presented. In chronoamperometric (CA) measurements, first the potential was dropped in steps from open circuit potential to 0.45 V for 1 h. Nitrogen gas was bubbled prior to experiments for 15 min and purged over the solution during the experiment. Current densities were normalized by the electrochemically accessible surface area (SA) from H_{UPD} stripping.

3. RESULTS AND DISCUSSION

Five binary and ternary nanoparticle electrocatalysts were studied to clarify synergistic effects of an atomic vicinity of Pt, Rh, and Sn sites (Table 1). The electrocatalysts will henceforth be referred to using a nomenclature that includes the sequence of addition of the precursor materials. The "+" symbol indicates a stepwise addition. Thus, the ternary "PtRhSn/C" catalyst (catalyst 2 in Table 1) was prepared by simultaneous reduction, whereas for the ternary "Sn+Rh+Pt/C" catalysts, each precursor was added and reduced separately from left to right. Similarly, for the Sn+RhPt/C catalyst, Sn was reduced first, followed by simultaneous addition of Rh and Pt. The two binary catalysts Sn+Pt/C and PtRh/C were prepared accordingly as reference materials.

The molar ratio of Pt/Rh/Sn was maintained at previously optimized ratios for high ethanol oxidation activity.[12] Pt/Rh ratio in catalyst 1 was 3:1, and Pt/Sn in catalyst 5 was kept close to 1:1. We expected the possibility of homogeneous single phase formation upon coreduction of all three components (catalyst 1), whereas multiphases were likely outcomes for the stepwise materials. We note that Pt, Rh, and Sn have very close atomic radii of 2.76, 2.69, and 2.80 Å, respectively. By reducing the Sn precursor first, followed by Rh and/or Pt, we systematically explored previously overlooked effects of the order of precursor addition on the detailed atomic distribution at bulk and interface and its critical effect on structure and catalytic activity.

3.1. Composition and Morphology. ICP-OES analysis and EDX measurements confirmed chemical compositions of catalysts 2, 3, and 4 close to the targeted values regardless of the sequence of addition employed. The weight percent metal loading of catalysts on carbon support was also obtained from ICP-OES and independently cross-confirmed by EDX. The chemical composition (in terms of atomic ratios) and metal loading of the catalysts are shown in Table 1.

TEM micrographs of the electrocatalysts (Figure 1) evidenced that the nanoparticles were well-distributed across the carbon support and largely spherical in shape with sizes ranging from 9 to 20 nm. The metal loadings ranged from 22 to 42% by weight. Mean particle diameters were estimated from TEM-derived size distribution histograms and are shown in Figure S1.

3.2. Atomic-Scale Structure. Conventional Cu Kα XRD and synchrotron-based HE-XRD studies coupled to atomic pair distribution function (PDF) analysis was used to study the atomic-scale structural properties of all five electrocatalysts. XRD patterns are shown in Figure 2 and show relatively broad

Table 1. Size, Molar Composition, and Metal Weight Loading of the Supported PtRhSn Electrocatalysts[a]

catalysts	atomic ratio (Pt/Rh/Sn)	total metal loading wt %	average particle size (nm)
(1) PtRh/C	74:26:0	35.0	17.8 ± 7.3
(2) PtRhSn/C	41:9:50	33.9	9.0 ± 2.9
(3) Sn+Rh+Pt/C	46:7:47	28.5	18.9 ± 4.8
(4) Sn+RhPt/C	45:8:47	21.9	15.9 ± 4.7
(5) Sn+Pt/C	56:0:44	42.1	12.8 ± 2.6

[a]The + sign indicates a stepwise addition and reduction of precursors.

Bragg peaks, typical for nanosized particles with limited structural coherence. Still the peak patterns reveal important insight how the synthesis protocol affected the resulting bulk structure. The reflections of the PtRh/C catalysts suggest an essentially phase-pure Pt–Rh bimetallic phase. Both Pt and Rh show a face-centered cubic (fcc) space group $Fm3m$ with very similar lattice constants of 3.9231 and 3.8031 Å, respectively. This favors the formation of homogeneous PtRh binary solid solutions over wide compositional ranges, as indicated by the Pt–Rh phase diagram.[11] This is why Pt and Rh diffraction peaks cannot be resolved separately in any of the XRD patterns. The (111) reflection was found between the Pt (111) and Rh (111) literature values of 39.764 and 41.069°, respectively, evidence alloy formation and bulk lattice compression compared to pure Pt.

Interestingly, the pattern of PtRhSn/C catalyst shows no peaks coinciding in position with those of the PtRh/C catalyst. This indicates the formation of an entirely new homogeneous phase with a characteristic peak pattern that can unambiguously be attributed to a hexagonal PtSn phase known as the mineral Niggliite (Table S1). Given the chemical presence of Rh in the
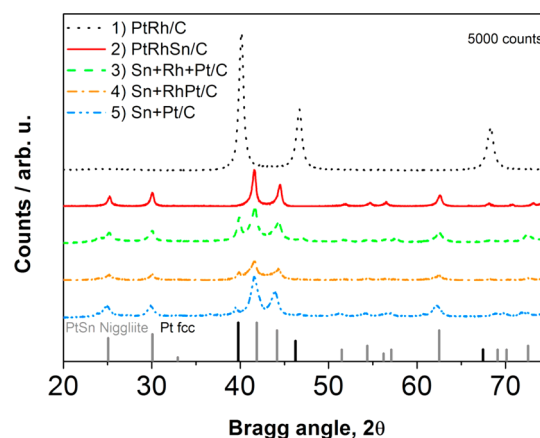

Figure 2. Cu Kα XRD pattern of different catalyst: (1) PtRh/C, (2) PtRhSn/C, (3) Sn+Rh+Pt/C, (4) Sn+RhPt/C, and (5) Sn+Pt/C. Pure Pt fcc and pure PtSn-Niggliite diffraction patterns are indicated in black and gray lines, respectively.

catalyst PtRhSn/C, the XRD pattern suggests that Rh atoms are substitutionally incorporated into the Niggliite lattice.

The other Sn-containing catalysts also reveal the presence of the Niggliite phase, however, and show a secondary phase Pt or PtRh phase with additional reflections around $2\theta \sim 40°$. Thus, stepwise precursor addition caused segregated metallic alloy phases. The presence of Rh (see Sn+Rh+Pt/C and Sn+RhPt/C) contracts the lattice of the secondary Pt phase and shifts its reflections to higher angles. Although absent in the XRD pattern of Figure 2, the presence of minor nanocrystalline or amorphous SnO_x phases, especially near the surface, cannot be ruled out.

To explore the 3D atomic arrangement of Pt, Rh, and Sn atoms regardless of their structural coherence (i.e., for both
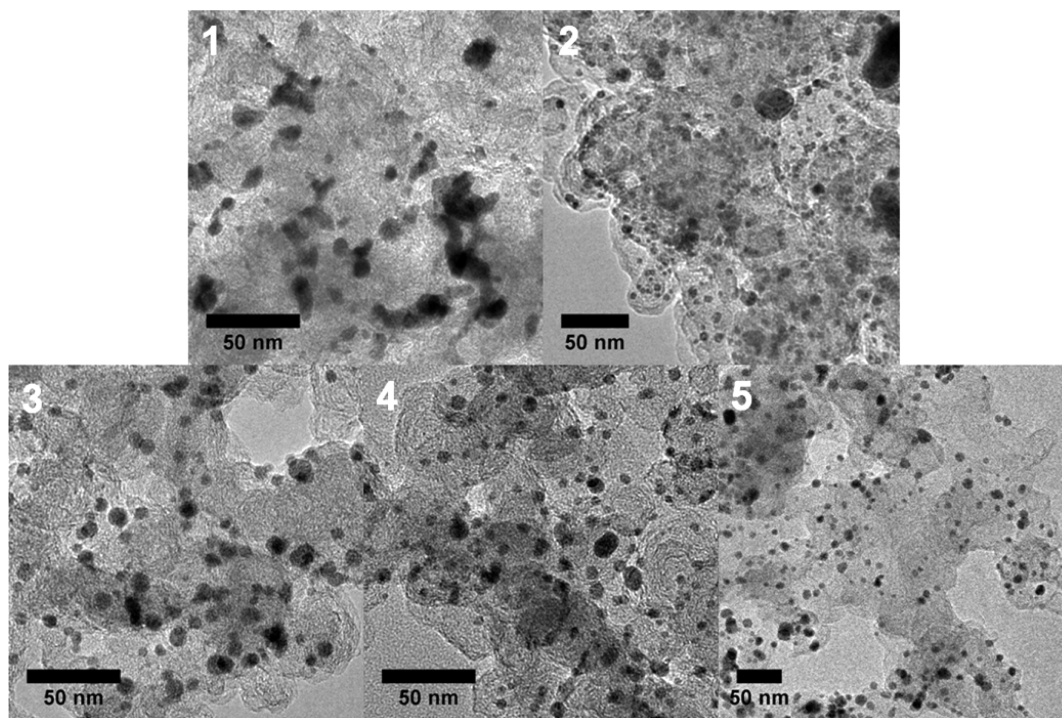

Figure 1. TEM micrographs of electrocatalyst: (1) PtRh/C, 17.8 ± 7.3 nm; (2) PtRhSn/C, 9.0 ± 2.9 nm; (3) Sn+Rh+Pt/C, 18.9 ± 4.8 nm; (4) Sn+RhPt/C, 15.9 ± 4.7 nm; and (5) Sn+Pt/C, 12.8 ± 2.6 nm.

nanocrystalline or amorphous phases), we conducted synchrotron-based HE-XRD experiments coupled to atomic pair distribution functions (PDF) analysis. HE-XRD and atomic PDFs are rapidly emerging as a very efficient technique in studying the atomic-scale structure of nanosized materials.[26,27] A set of synchrotron HE-XRD patterns collected at $\lambda = 0.1080$ Å is shown in Figure 3A. The atomic PDFs extracted from the
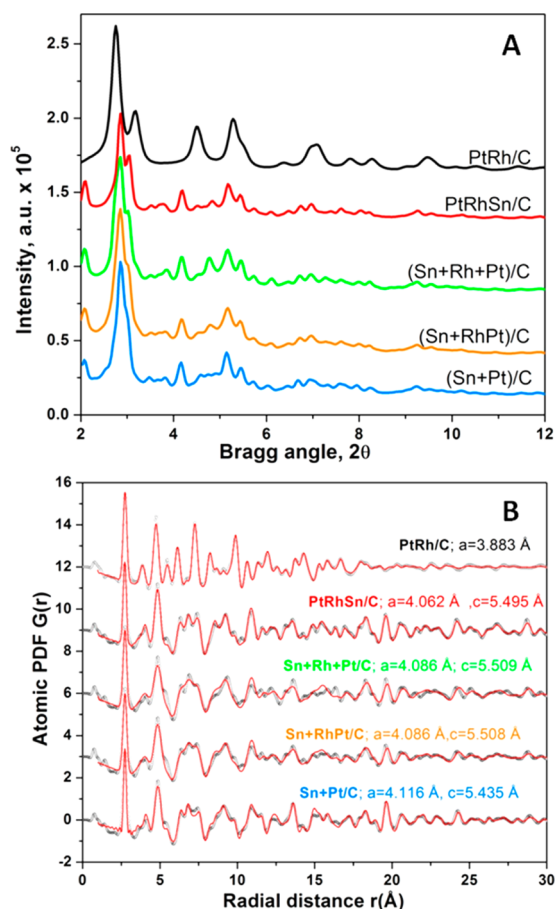

Figure 3. (A) Synchrotron-based HE-XRD patterns collected at $\lambda = 0.1080$ Å of (1) PtRh/C, (2) PtRhSn/C, (3) Sn+Rh+Pt/C, (4) Sn+RhPt/C, and (5) Sn+Pt/C. (B) Atomic pair distribution functions (PDFs) derived from the XRD patterns (gray symbols) and computed from structure models (red solid lines). The refined lattice parameters are given by each data set.

synchrotron XRD patterns are shown by the gray scatter points in Figure 3B. By definition, experimental PDFs show positive peaks at distances separating pairs of atoms (i.e., where the local atomic density exceeds the average one). From these data, we can derive the immediate coordination of each atom in the entire 3D lattice, which provides the full atomic 3D structure of the nanocatalysts. The one-dimensional attenuations in the PDF ultimately die down to around zero at the structural coherence length (crystallite size) of the catalysts. Inspection of the peak envelopes evidence that all catalysts show nanocrystalline structures with coherence lengths between 15 and 20 Å.

To derive real-space 3D structural motifs of the catalyst phases, computational PDFs based on suitable structural models of PtRh- and Sn-containing phases were fitted to the experimental PDFs. The PDF of the PtRh/C catalyst (Figure 3B) can be approximated with a structure model featuring a

face-centered-cubic (fcc) lattice occupied by Rh and Pt atoms in a random manner (Figure 4). The PDFs for the Sn-
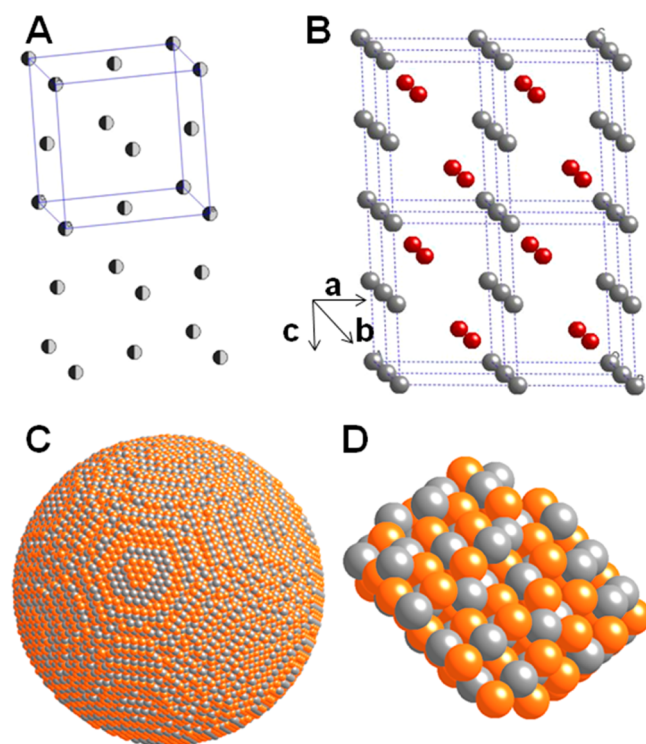

Figure 4. (A) PDF-derived 3D structural model of a fcc lattice, randomly occupied by Rh and Pt atoms (gray balls). Unit cell is given by lines. (B) A hexagonal, Niggliite structure featuring alternating layers of Pt (gray balls) and Sn (red balls) atoms. Spherical model of Niggliite structured particle (C) and excerpt of the particle surface (D) with Sn (orange balls) and Pt sites (gray balls) doped randomly with Rh (also gray balls).

containing catalysts, on the other hand, are well-approximated by a model featuring a hexagonal lattice of the type found in the mineral Niggliite with an overall Pt_1Sn_1 stoichiometry and where Rh atoms randomly replace Pt atoms. Fitted unit cell parameters are shown in Figure 3B, indicating that the fcc unit cell parameter of the PtRh/C catalyst (3.883 Å) is smaller than that of pure Pt 3.910 Å, commensurate with a lattice-contracted disordered alloy. The differences in the PDF peak oscillation pattern between PtRh/C and the four Sn-containing materials (see, for instance, in the 5−10 Å range) underscore their distinctly different structural atomic arrangement. The Sn-containing catalysts show similar oscillations, radial distances, and short-order crystallinity. Structural differences manifest themselves largely in variations of the unit cell dimensions "a" and "c" (Figure 4). Close inspection of the PDF patterns reveals sharper and more intense PDF peaks for the PtRhSn/C catalyst compared to the other Sn-containing materials (e.g., at pair distances 4.5 and 11 Å). Seemingly a subtle difference, this important detail, however, hints to enhanced structural order in surface and bulk.

In light of the structural analysis, XRD and HE-XRD/PDF evidence the prevalent formation of a ternary substitutional solid solution consisting of Sn, Pt, and Rh with Niggliite structure. Increasing phase homogeneity upon simultaneous addition of precursors resulted in increasing lattice contraction and structural order. The surface of the Niggliite particles is illustrated in Figure 4C and 4D. It exposes Sn, Pt, and the

doped Rh atoms in close vicinity with a high concentration of active ternary sites for the ethanol oxidation.

3.3. Electrocatalytic Ethanol Oxidation Activity.

To correlate catalyst structure and composition with the electrocatalytic EOR polarization behavior, cyclic voltammograms in 0.5 M H_2SO_4 (Figure S3) and linear sweep voltammograms (LSVs) in 0.5 M H_2SO_4 and 0.5 M C_2H_5OH (Figure 5) were
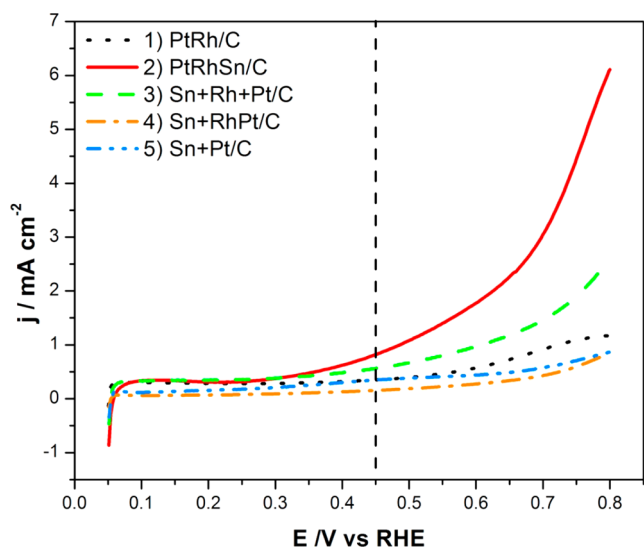

Figure 5. Polarization curves of the electrocatalytic ethanol oxidation reaction (EOR): (1) PtRh/C, (2) PtRhSn/C, (3) Sn+Rh+Pt/C, (4) Sn+RhPt/C, and (5) Sn+Pt/C recorded in 0.5 M H_2SO_4 and 0.5 M C_2H_5OH. Current densities are normalized by the electrochemically accessible surface area (SA) from H_{UPD} stripping with a scan rate of 20 mV/s. The vertical dashed line marks the potential of the chronoamperometric experiment in Figure 6

collected. In addition, potentiostatic chronoamperometric (CA) experiments were performed to examine the catalytic performance and catalyst stability at an electrode potential of technical interest for extended period of times (Figure 6). Current densities were normalized by the electrochemically
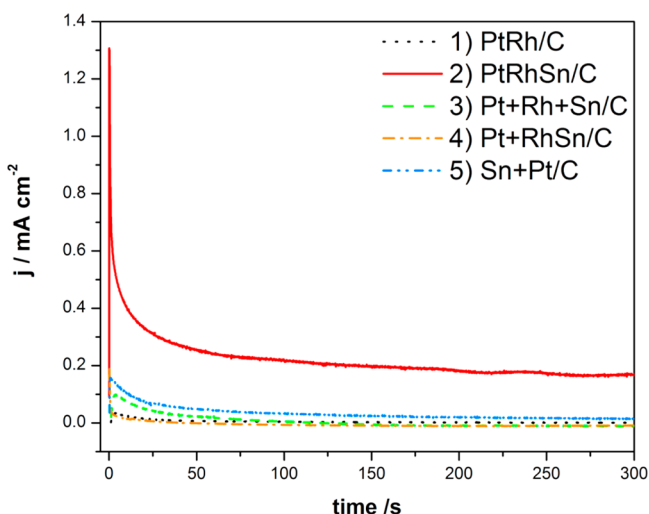

Figure 6. Potentiostatic chronoamperometry of the Pt−Rh−Sn/C electrocatalysts at E = +0.45 V vs RHE recorded in 0.5 M H_2SO_4 and 0.5 M EtOH. Current densities are normalized by the electrochemically accessible surface area (SA) from H_{UPD} stripping.

accessible surface area (SA) from H_{UPD} stripping. Table 2 reports relevant experimental activity data. Additional activity and current density data relative to the ECSA and the Pt mass are reported in Table S3.

Clearly, the single-phase PtRhSn/C catalyst dramatically outperformed the other catalysts, both under potentiodynamic scan and under potentiostatic test conditions. This suggests that the homogeneous Rh-doped Pt−Sn Niggliite structure (Figure 3) must have formed the catalytically most active surface sites under reactive conditions. Our bulk structural conclusions yield only limited clues about the atomic structure of possible active crystal surfaces. Although in principle controlled by the bulk structure, the active surface depends on a large number of additional factors such as crystal facet orientation, compositional segregation of elements, or partial loss of crystal ordering during reactive conditions. The surface chemistry is discussed in detail in the later section 3.4.

The presence of a secondary PtRh metallic alloy phase, as seen for catalysts 3, 4, and 5 in Figure 2, proved without exception detrimental to the experimental catalytic activity. This appears plausible considering that phase-separated Pt/Rh metal atoms are lost for the formation of active ternary active sites on the surface of Niggliite phases. PtRh alloy sites without atomic neighborhood of oxophilic Sn species may activate ethanol, yet lack sufficient active oxygenates to efficiently remove carbonous adsorbates resulting in lower catalytic activity.

A similar conclusion can be drawn from the comparison of the two binary catalysts, PtRh/C and Sn+Pt/C. Well-alloyed PtRh/C fails to maintain sustained EOR activities, likely due to rapid buildup of tightly bound carbonous surface species. The lower activity of Sn+RhPt/C as the Sn+Pt/C catalyst indicates that the beneficial effect of Rh itself may contribute to the overall activity, but it is influencing predominantly the selectivity toward CO_2. This confirms earlier reports on the beneficial role of Sn species in the oxidation of organic molecules.

Although the general beneficial effect of Rh for C−C bond splitting has been well-documented,[28,29] the relative activities of Sn+RhPt/C and Sn+Pt/C strongly evidence that the detailed chemical and structural state of Rh atoms is critical to fully unfold activity enhancements.

The structure−activity relations of the single-phase Rh-doped Niggliite structure (PtRhSn/C) are consistent with an earlier hypothesis[8] about the beneficial effect of a "quasi random PtRhSn alloy". However, the present Rh-doped Niggliite electrocatalysts displayed 4 and 5 times higher current densities at +0.45 V and +0.6 V, respectively, than a similar $PtRhSnO_2/C$ catalyst.[15] Improved EOR activity was also observed in comparison to an earlier PtRhSn catalyst with the same 3:1:4 ratio,[12] and compared to a Rh-content optimized Rh-PtSn/C catalyst.[16]

3.4. Surface Chemistry of the Most Active PtRhSn/C Catalyst.

PtRhSn/C catalysts were studied by XPS before acid exposure (BAE) and after acid exposure (AAE) under EOR reaction conditions. The Pt 4f, Rh 3d, and Sn 3d spectra (Figure S2) were very similar before and after acidic exposure, with Pt being essentially metallic and Sn existing largely in a SnO_2 state near the surface. The low binding energy shoulder at ~485 eV indicated some metallic contribution. As Sn was unlikely to be in the elemental Sn state, the most likely scenario is the formation of a Rh-doped Pt−Sn alloy in the near-surface region, consistent with the XRD and HE-XRD results in the

Table 2. Electrochemical EOR Activity of Pt−Rh−Sn/C Catalysts[a]

catalyst	ECSA $cm^2 \cdot mg_{Pt}^{-1}$	i @ 0.45 V mA cm^{-2}	i @ 0.60 V mA cm^{-2}	i @ 0.45 V@300 s mA cm^{-2}
(1) PtRh/C	10.7	0.35	0.58	7.02×10^{-4}
(2) PtRhSn/C	26.5	0.82	1.78	1.66×10^{-1}
(3) Sn+Rh+Pt/C	12.1	0.57	0.97	∼0
(4) Sn+RhPt/C	33.5	0.15	0.27	∼0
(5) Sn+Pt/C	15.5	0.35	0.44	1.50×10^{-2}

[a]Electrochemical surface area (ECSA), current densities at 0.45 V vs RHE and 0.6 V vs RHE during voltammetric scans, and current density at constant 0.45 V vs RHE after 300 s.

bulk. Rh 3d (5/2) spectra at ∼310 eV suggested the presence of metallic Rh. A slight presence of oxide (Rh_2O_3) is observed after acid treatment. The quantitative elemental composition is provided in Table S2. These data show a constant (Pt + Rh)/ Sn ratio near the surface and some small loss of precious metals and Sn upon acid treatment. Converted into relative molar ratios, the near surface composition of the Niggliite phase before acid treatment was about Pt/Rh/Sn = 66:25:9 and changed only very slightly after acid treatment to 68:23:9. This suggests that the original Niggliite bulk phase with molar ratio of Pt/Rh/Sn = 41:9:50 transformed into SnO_2 and a noble metal-enriched phase at the surface due to the exposure to air and aqueous electrolyte. There is a notable increase of the oxygen content of the AAE sample, probably due to functionalization of the carbon support.

From the XPS data, we conclude that the active surface of the bulk single-phase Niggliite PtRhSn/C catalyst evolved into active catalytic sites characterized by uniformly distributed metallic Pt, Sn, and Rh surface sites in atomic neighborhood to oxophilic surface SnO_2. These are supported on the homogeneous bulk Pt−Rh−Sn Niggliite phase. The close interaction of the Pt/Rh/Sn and SnO_2 moieties appears instrumental in the high electrocatalytic activity performance.

3.5. Reaction Intermediates and CO_2 Selectivity. Mechanistic aspects, including reactive surface intermediates and products of the EOR on the active Rh-doped Niggliite phase electrocatalyst (PtRhSn/C) was studied using in situ FTIR. Special emphasis was placed on an analysis of whether ethanol can be oxidized in a 12 electron pathway to CO_2. Figure 7 reports in situ SNIFTIRS spectra of the intermediates
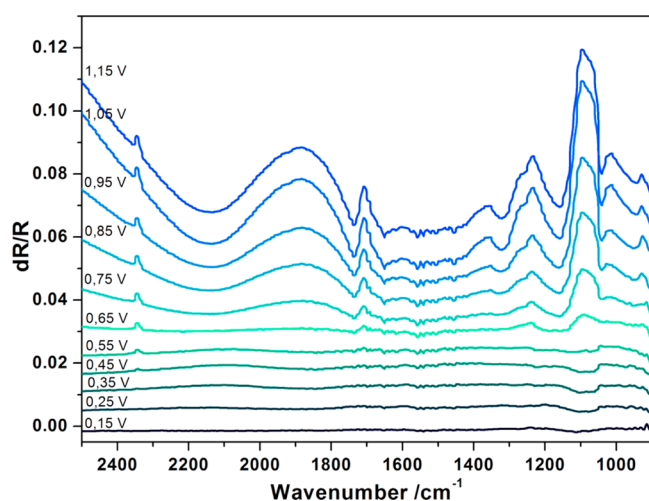

Figure 7. SNIFTIRS spectra during ethanol oxidation on PtRhSn/C between +0.15 V and +1.15 V vs RHE. Conditions: 0.1 M $HClO_4$ + 0.5 M C_2H_5OH. The spectrum at +0.10 V is used as background.

and products during ethanol oxidation between +0.15 V to +1.15 V versus RHE. Following earlier analyses under similar conditions, we assign the following bands: around 2300 cm^{-1} to the asymmetric CO_2 stretching mode; around 1700 cm^{-1} to C=O stretching in acetic acid and acetaldehyde; around 1390−1410 cm^{-1} to O−C−O stretching of adsorbed acetate; around 1350 cm^{-1} to CH_3 in-plane bending mode; around 1280 cm^{-1} to C−O stretching of acetic acid; around 900 cm^{-1} to the C−C−O asymmetric stretching of acetaldehyde; and the broad band at 1100 cm^{-1} to ClO_4^-.[30]

The in situ FTIR data in Figure 7 provide evidence for the formation of CO_2 during EOR as a result of C−C bond splitting in ethanol by a 12 electron oxidation process. CO_2 evolution commences as early as 0.45 V and gradually increases with electrode potential. This is, to our knowledge, one of the earliest onset of the 12 electron oxidation pathway reported in the literature.[8,12,16] Characteristic peaks stemming from acetic acid and acetaldehyde suggested partial incomplete oxidation. Hence, like most other earlier materials the Niggliite phase of the PtRhSn/C catalyst induces both C−C bond splitting (complete oxidation) and partial oxidation of ethanol.

4. CONCLUSIONS

We have presented the synthesis, the structural bulk and surface characterization, and the electrocatalytic activity and selectivity of nanostructured ternary Pt−Rh−Sn materials in defined stoichiometric ratios. Unlike earlier studies, we have placed special emphasis on the exploration of the detailed 3D atomic arrangement and chemical surface states of the catalytically active phases and components; we also addressed the previously overlooked question as to the order in which the ternary catalysts were assembled in the synthetic process.

Scattering data and atomic PDF analysis revealed, for the first time, a single-phase Rh-doped Pt−Sn Niggliite structure as the preferred and catalytically most active nanocrystalline phase. On its surface, metallic Pt and Rh are atomically mixed with a SnO_2 phase, giving rise to active-surface-site ensembles. Only owing to simultaneous reduction of all three precursors was the phase-pure ternary Niggliite phase experimentally accessible. Secondary PtRh metal alloy phases proved detrimental to catalytic activity. The EOR activity of the homogeneous Niggliite material outperformed a previous EOR catalyst of the PtRhSn family. In situ spectroscopy confirmed the favorable activity by an early CO_2 onset potential of the complete 12 electron oxidation pathway.

Our structural conclusions as to the active catalytic phase represent a significant step forward in our understanding of structural and mechanistic aspects of this class of catalytic materials. The present methodologies and structural insights will aid in the materials-by-design approach for further improved direct ethanol fuel cell (DEFC) catalysts as well as for catalysts for the oxidation of liquid small organics in general.

■ ASSOCIATED CONTENT

Ⓢ Supporting Information

Mean particle diameter and size distribution histograms of electrocatalysts, 2θ values of electrocatalysts in comparison with tabulated diffraction patterns, XP spectra for PtRhSn/C and quantitative analysis of the XPS peaks, cyclic voltammograms of electrocatalysts in pure electrolyte, electrocatalytic activity relative to ECSA and mass. This material is available free of charge via the Internet at http://pubs.acs.org.

■ AUTHOR INFORMATION

Corresponding Author

*E-mail: pstrasser@tu-berlin.de.

Author Contributions

#Both authors (N.E. and R.L.) have made an equal contribution to this paper

Notes

The authors declare no competing financial interest.

■ ACKNOWLEDGMENTS

■ REFERENCES

(1) Antolini, E. *J. Power Sources* **2007**, *170*, 1−12.

(2) Wang, H.; Jusys, Z.; Behm, R. J. *J. Phys. Chem. B* **2004**, *108*, 19413−19424.

(3) de Souza, J. P. I.; Queiroz, S. L.; Bergamaski, K.; Gonzalez, E. R.; Nart, F. C. *J. Phys. Chem. B* **2002**, *106*, 9825−9830.

(4) Linares, J. J.; Rocha, T. A.; Zignani, S.; Paganin, V. A.; Gonzalez, E. R. *Int. J. Hydrogen Energy* **2013**, *38*, 620−630.

(5) Zhou, W.; Zhou, Z.; Song, S.; Li, W.; Sun, G.; Tsiakaras, P.; Xin, Q. *Appl. Catal., B* **2003**, *46*, 273−285.

(6) Hitmi, H.; Belgsir, E. M.; Leger, J. M.; Lamy, C.; Lezna, R. O. *Electrochim. Acta* **1994**, *39*, 407−415.

(7) Iwasita, T.; Pastor, E. *Electrochim. Acta* **1994**, *39*, 531−537.

(8) Kowal, A.; Li, M.; Shao, M.; Sasaki, K.; Vukmirovic, M. B.; Zhang, J.; Marinkovic, N. S.; Liu, P.; Frenkel, A. I.; Adzic, R. R. *Nat. Mater.* **2009**, *8*, 325−330.

(9) Colmati, F.; Antolini, E.; Gonzalez, E. R. *Appl. Catal., B* **2007**, *73*, 106−115.

(10) Song, S.; Tsiakaras, P. *Appl. Catal., B* **2006**, *63*, 187−193.

(11) Colmati, F.; Antolini, E.; Gonzalez, E. R. *J. Alloys Compd.* **2008**, *456*, 264−270.

(12) Li, M.; Kowal, A.; Sasaki, K.; Marinkovic, N.; Su, D.; Korach, E.; Liu, P.; Adzic, R. R. *Electrochim. Acta* **2010**, *55*, 4331−4338.

(13) Spinace, E. V.; Dias, R. R.; Brandalise, M.; Linardi, M.; Neto, A. O. *Ionics* **2010**, *16*, 91−95.

(14) Silva, J. C. M.; Parreira, L. S.; De Souza, R. F. B.; Calegaro, M. L.; Spinacé, E. V.; Neto, A. O.; Santos, M. C. *Appl. Catal., B* **2011**, *110*, 141−147.

(15) Kowal, A.; Gojković, S. L.; Lee, K. S.; Olszewski, P.; Sung, Y. E. *Electrochem. Commun.* **2009**, *11*, 724−727.

(16) García-Rodríguez, S.; Rojas, S.; Peña, M. A.; Fierro, J. L. G.; Baranton, S.; Léger, J. M. *Appl. Catal., B* **2011**, *106*, 520−528.

(17) Zhu, M.; Sun, G.; Xin, Q. *Electrochim. Acta* **2009**, *54*, 1511−1518.

(18) Kim, J. H.; Choi, S. M.; Nam, S. H.; Seo, M. H.; Choi, S. H.; Kim, W. B. *Appl. Catal., B* **2008**, *82*, 89−102.

(19) Purgato, F. L. S.; Olivi, P.; Léger, J. M.; de Andrade, A. R.; Tremiliosi-Filho, G.; Gonzalez, E. R.; Lamy, C.; Kokoh, K. B. *J. Electroanal. Chem.* **2009**, *628*, 81−89.

(20) Liu, Z.; Hong, L.; Tay, S. W. *Mater. Chem. Phys.* **2007**, *105*, 222−228.

(21) Lim, D.-H.; Choi, D.-H.; Lee, W.-D.; Lee, H.-I. *Appl. Catal., B* **2009**, *89*, 484−493.

(22) De Souza, R. F. B.; Parreira, L. S.; Rascio, D. C.; Silva, J. C. M.; Teixeira-Neto, E.; Calegaro, M. L.; Spinace, E. V.; Neto, A. O.; Santos, M. C. *J. Power Sources* **2010**, *195*, 1589−1593.

(23) Du, W.; Wang, Q.; LaScala, C. A.; Zhang, L.; Su, D.; Frenkel, A. I.; Mathur, V. K.; Teng, X. *J. Mater. Chem.* **2011**, *21*, 8887−8892.

(24) Petkov, V. *Synchrotron Radiation News* **2009**, *22*, 29−33.

(25) Pettinger, B.; Lipkowski, J.; Hoon-Khosla, M. *J. Electroanal. Chem.* **2001**, *500*, 471−478.

(26) Loukrakpam, R.; Shan, S.; Petkov, V.; Yang, L.; Luo, J.; Zhong, C.-J. *J. Phys. Chem. C* **2013**, *117*, 20715−20721.

(27) Loukrakpam, R.; Wanjala, B. N.; Yin, J.; Fang, B.; Luo, J.; Shao, M.; Protsailo, L.; Kawamura, T.; Chen, Y.; Petkov, V.; Zhong, C.-J. *ACS Catal.* **2011**, *1*, 562−572.

(28) Li, M.; Zhou, W. P.; Marinkovic, N. S.; Sasaki, K.; Adzic, R. R. *Electrochim. Acta* **2013**, *104*, 454−461.

(29) Teran, F. E.; Santos, D. M.; Ribeiro, J.; Kokoh, K. B. *Thin Solid Films* **2012**, *520*, 5846−5850.

(30) Konopka, D. A.; Li, M.; Artyushkova, K.; Marinkovic, N.; Sasaki, K.; Adzic, R.; Ward, T. L.; Atanassov, P. *J. Phys. Chem. C* **2011**, *115*, 3043−3056.